Chemical Evolution via Beta Decay: A case study in Strontium-90

N. A. Marks, D. J. Carter, M. Sassi

Nanochemistry Research Institute, Curtin University, GPO Box U1987, Perth
WA 6845, Australia

A. L. Rohl

Nanochemistry Research Institute, Curtin University, GPO Box U1987, Perth
WA 6845, Australia
iVEC, 26 Dick Perry Ave, Kensington WA 6151, Australia

K. E. Sickafus, B. P. Uberuaga, C. R. Stanek

Materials Science and Technology Division, Los Alamos National Laboratory,
Los Alamos, NM 87545, USA

E-mail: `N.Marks@curtin.edu.au`

Abstract. Using ^{90}Sr as a representative isotope, we present a framework for
understanding beta-decay within the solid state. We quantify three key physical
and chemical principles, namely momentum-induced recoil during the decay event,
defect creation due to physical displacement, and chemical evolution over time.
A fourth effect, that of electronic excitation, is also discussed but this is difficult
to quantify and is strongly material-dependent. The analysis is presented for the
specific cases of $SrTiO_3$ and SrH_2. By comparing the recoil energy with available
threshold displacement data we show that in many beta-decay situations defects
such as Frenkel pairs will not be created during decay as the energy transfer is
too low. This observation leads to the concept of chemical evolution over time
which we quantify using density functional theory. Using a combination of Bader
analysis, phonon calculations and cohesive energy calculations, we show that beta-
decay leads to counter-intuitive behavior which has implications for nuclear waste
storage and novel materials design.

1. Introduction

The management of radioactive waste remains a major social, political and technological challenge. A critical scientific contribution to this problem is the development of robust materials science solutions that encapsulate radioisotopes for long periods of time. Many decades of research have been devoted to the development of suitable materials. These programs have typically emphasized the ability of the host phase to accommodate fission products and to resist leaching into the environment. One of the most widely studied physical effects has been the response of the material to radiation damage arising from alpha-decay of actinides (see Refs. [1, 2] for reviews on crystalline oxide wasteforms as relevant to this study). Due to conservation of momentum, these high-energy alpha particles ($Q \approx 4$ MeV) give rise to recoil of the daughter nucleus with an energy of around 80 keV, sufficient to temporarily disrupt many thousands of atoms from their lattice sites. The critical question from a nuclear waste perspective is whether or not the host material is structurally destabilized by these processes. Some materials have exceptional radiation tolerance and can retain their crystallinity up to very high doses, while others transform under irradiation to an amorphous/metamict phase in which swelling and cracking become possible [3].

Recent studies by ourselves [4, 5, 6] and others [7, 8, 9] have examined several nuclear materials systems in which alpha-decay is not present and the only radioactive process is beta-decay. These works were motivated by modern considerations in nuclear waste storage such as the recent work of Wigeland *et al.* [10] who showed that geological repositories could increase their capacity by more than a hundred-fold if a handful of critical isotopes were chemically extracted from the spent nuclear fuel. There are two main isotope groups in question: (i) "short-lived" beta-emitters, ^{137}Cs and ^{90}Sr, with a half-life of around 30 years, and (ii) transuranics, principally Pu, Am and Cm. This insight motivates the design of wasteforms specifically targeted at beta-emitters. Our first study of this process [4] employed density functional theory to study the decay of ^{137}CsCl to rocksalt ^{137}BaCl, revealing unexpected chemistry associated with chemical evolution. Drawing on related concepts in mineralogy and geology, we termed (in Ref. [5]) this process radioparagenesis, in which a solid-state daughter phase is derived radiogenically from a parent phase. Radioparagenesis not only opens the possibility of creating novel materials but also suggests a backwards-design philosophy for nuclear wasteform in which the host phase becomes more stable over time. Both of these principles have been explored in our recent publications [5, 6] and experiments are presently underway to test the concept in the laboratory. Related experiments by Jiang *et al.* [7, 9] have also been performed employing ion beams to implant Zr and O ions into SrTiO$_3$.

The critical underlying principle of radioparagenesis is that beta-decay is fundamentally different to alpha-decay from a radiation effect perspective; as noted by Robinson [11], very little structural damage is produced by beta-decay. In beta-decay three critical processes occur: (i) a new chemical species is created, (ii) the nucleus recoils due to the emission of the beta particle and neutrino, and (iii) the beta particle deposits its kinetic energy into the surrounding material. The first two of these processes are *local*, affecting the immediate environment of the transmuted nucleus; these processes can be quantified precisely and are the primary focus of this work. The third process, involving the interaction between the beta-particle and the surrounding material, occurs over a much larger length-scale, with a beta-particle typically travelling several millimetres in solids [12]. The beta-particle slows down due

to a combination of nuclear and electronic processes which lead to variety of effects including displacement of atoms from their lattice site, the creation of excitons and the production of secondary electrons and photons. Some of these electronic processes can in turn generate defects through the decay of excitons, with alkali halides being the prototypical example [13]. An important point in the context of this work is that the total electronic stopping power is rather small, being less than 0.1 eV/Å for a beta-particle with an energy of 1 MeV [14]. Accordingly, the beta-particle has a comparatively small effect on the length scale of the transmuted nucleus.

This article presents the critical processes which underpin the radioparagenesis concept, using the ^{90}Sr isotope as the primary vehicle for discussion. The half-life of ^{90}Sr is 29.8 years, beta-decaying to ^{90}Y, which in turn beta-decays to stable ^{90}Zr with a half-life of 64 hours. The large chemical difference (in radius and formal oxidation state) between the parent radioisotope and the stable daughter makes ^{90}Sr an appealing example of the radioparagenesis process. Section II introduces the principles of daughter recoil within beta-decay, showing the dependence of the recoil energy on the beta energy spectrum and the nature of the decay process. Section III places these recoil energies in the context of physical processes within the solid state, employing threshold displacement energies which can be computed using molecular dynamics simulation. We also briefly discuss electronic processes associated with the passage of the beta particle through the material, noting that quantification of the number, location and type of defects arising from a single beta-particle is unachievable. Section IV summarizes the effects of chemical evolution in two prototypical solids (perovskite $SrTiO_3$ and cotunnite SrH_2) in which the radioactive parent phase contains exclusively ^{90}Sr. Due to the short half-life of the intermediate ^{90}Y daughter, we consider only the stable Zr species when studying chemical evolution, since the Y species are present in negligible concentrations relative to the other species.

2. Recoil Induced by Beta Decay

Due to conservation of energy and momentum, it is elementary that the daughter nucleus will recoil following beta-decay. Less obvious is the shape and magnitude of the energy spectrum of the recoiling daughter nucleus. Indeed, there are very few measurements of the beta-recoil spectrum in solids due to the problem of scattering; early measurements [15, 16] considered gaseous species such as ^{6}He, ^{19}Ne, ^{23}Ne and ^{35}Ar to avoid this problem. Presently, the WITCH experiment [17, 18, 19] at CERN is seeking to measure the recoil energy spectrum of daughter nuclei using a Penning trap. For the present discussion we will for simplicity presume an isotropic angular distribution between the beta particle and neutrino, although in reality the situation is more complex due to the specifics of the weak interaction; indeed, the WITCH experiments will measure very small differences in the recoil energy spectrum (see Fig. 1 in Ref. [17]) to discern the admixture of additional interactions beyond the predominant V-A (vector/axial vector) character.

Here we compute the daughter recoil energy (E) by convolving the measured beta energy spectrum [Fig. 1(a)] with a probability distribution which depends on the kinetic energy of the beta-particle, T_e. The maximum recoil kinetic energy occurs when the electron/positron receives all of the energy associated with the beta-decay, that is, $T_e=Q$, where Q is the end-point of the beta spectrum. According to relativistic
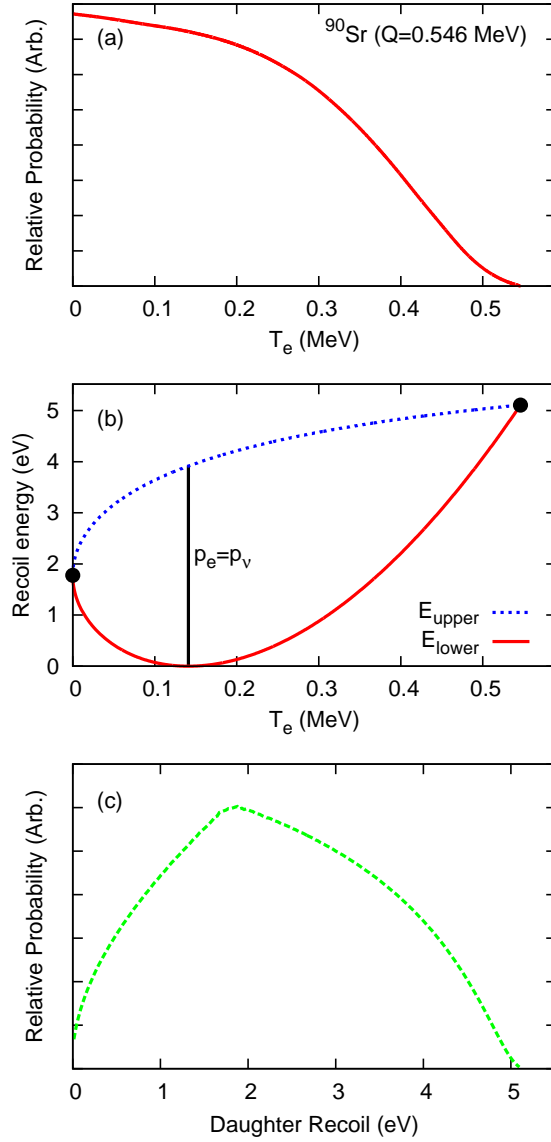
Figure 1. (a) Energy spectra for beta emission from ^{90}Sr. (b) Maximum and minimum recoil energies of the daughter nucleus as a function of the electron kinetic energy. (c) Daughter recoil energy spectrum for the case of an isotopic angular distribution between the neutrino and the beta electron.

kinematics, this value is given by the expression

$$E^{max} = \frac{Q(Q + 2mc^2)}{2Mc^2} \tag{1}$$

where c is the speed of light, and m and M are the masses of the electron and daughter nucleus, respectively. In the case of ^{90}Sr, for which Q=0.546 MeV, this amounts to a maximum recoil energy of 5.1 eV. The other limiting case occurs when the neutrino

receives all of the kinetic energy, in which case the daughter recoil is given by the expression

$$E^\nu = \frac{Q^2}{2Mc^2} \tag{2}$$

arising from $p_\nu c = Q$. For ^{90}Sr this case corresponds to a daughter recoil of just 1.8 eV, with the neutrino carrying off almost all of the energy due to its negligible mass. In all other cases the daughter recoil is more complicated due to the three-body nature of the decay. For a given value of T_e (intermediate between 0 and Q) the daughter recoil kinetic energy is dependent on the angle θ between the beta-particle and the neutrino, varying between two limits, E_{lower} and E_{upper} where

$$E_{\text{lower}} = \frac{(p_e - p_\nu)^2}{2M} \tag{3}$$

$$E_{\text{upper}} = \frac{(p_e + p_\nu)^2}{2M} \tag{4}$$

with the lower limit corresponding to $\theta = \pi$ and the upper limit to $\theta = 0$. The momenta p_e and p_ν are determined using relativistic kinematics and are given by

$$p_e = \sqrt{\frac{T_e^2}{c^2} + 2T_e m} \tag{5}$$

$$p_\nu = Q - T_e \tag{6}$$

thus ignoring the negligible mass of the neutrino and the very small contribution of the daughter nucleus to conservation of energy.

Fig. 1(b) shows the dependence of E_{lower} and E_{upper} on the beta-particle kinetic energy, with the limiting cases highlighted by solid circles. The vertical line at 0.14 MeV corresponds to the special case of $E_{\text{lower}} = 0$ which occurs when the magnitude of the beta-particle and neutrino momenta are the same. As can be seen by inspecting Eqs. 5 & 6, the energy at which this condition is met varies with Q.

Under the approximation that the angular correlation between the beta-particle and the neutrino is isotropic (a reasonable assumption which is sufficient for the present purposes) we can straightforwardly compute the distribution of recoil energies for a given value of T_e. Letting the angle between the neutrino and the beta-particle be θ, the recoil energy for a particular value of θ is given by

$$E(\theta) = \frac{p_e^2 + p_\nu^2 + 2p_e p_\nu \cos\theta}{2M} \tag{7}$$

where θ is uniformly distributed between 0 and π, corresponding to the azimuthal angle in spherical polar coordinates. Conveniently, the differential $dE/d\theta$ has a $\sin\theta$ dependance which is the same as the Jacobian [20], and hence the recoil energy E is distributed uniformly over the range between the two limits given in Eqs. 3 & 4. Convolving the beta-particle spectrum [Fig. 1(a)] with a uniform probability distribution between E_{lower} and E_{upper} as per Fig. 1(b) yields the daughter recoil spectrum shown in Fig. 1(c). The most probable recoil energy is around 1.85 eV, with the average being slightly higher at 2.3 eV due to the asymmetric shape of the distribution. As will be discussed in Sec. III, this energy is well below the threshold for creating Frenkel pairs, and hence beta-decay of ^{90}Sr within a lattice will not displace atoms via recoil.

Although the ^{90}Sr decay leads to a very low recoil process, the situation is somewhat different for the ^{90}Y$\rightarrow^{90}$Zr decay ($t_{1/2} = 64$ h) for which $Q = 2.280$ MeV.

Here the maximum recoil of the daughter is 45 eV and the average recoil is 25 eV. This highlights an important trend, namely that beta-decay with a high Q-value (or more precisely, a high end-point energy) will induce large recoils and vice-versa. Consequently, the highest energy recoils will occur for light radioisotopes with short half-lives.

While all of the above discussion applies equally to β^+ and β^- decay, the case of electron capture is slightly different, and in fact becomes kinematically trivial. For electron capture the recoil is a two-body process involving only the daughter nucleus and a neutrino. In such situations the daughter recoil energy has a specific value given by Eq. 2 and due to the negligible mass of the neutrino the recoil is maximally small. The same two-body kinematic argument applies for γ emission in which the massless photon removes almost all of the kinetic energy.

In the case of ^{137}Cs, a similar important isotope to ^{90}Sr in spent nuclear fuel, the predominant end-point for beta-emission is at 514 keV, even though the Q-value is 1.175 MeV. Accordingly, recoil during ^{137}Cs decay consists of two primary processes, a recoil of exactly 1.7 eV associated with the emission of a 662 keV γ, followed by a distribution of recoil energies associated with beta-decay. For the latter the maximum and average energies are 3.1 and 1.4 eV respectively.

3. Physical Processes and Creation of Defects

In the previous Section we considered the kinematics of beta-decay and showed that a daughter nucleus will typically recoil with a kinetic energy in the range of a few eV to several tens of eV. To put these recoil energies in a solid state context we need to consider defect formation processes in crystalline hosts. The principal quantity of interest is the threshold displacement energy, TDE, a material-specific property which quantifies the amount of energy required to permanently displace an atom from a lattice site. Despite their widespread use in ion implantation simulations, most typically in the binary collision SRIM program [21], determination of TDE's is extremely challenging from both an experimental and computational point of view.

Recently we computed TDE's for $SrTiO_3$ in the perovskite phase using molecular dynamics simulation [22]. The calculations employed a partial charge model [23] which has been subsequently shown to provide the most transferable description of $SrTiO_3$ systems amongst the models available [24]. Due to the computational cost of sampling all directions on the unit sphere, the calculations considered just the three main crystallographic directions in $SrTiO_3$. Even with this restriction, several hundred simulations were required, spanning a range of energies between 20 and 250 eV. The probability of forming a defect was extracted from the simulations and fitted with a Fermi-type function. Using a threshold definition of 50%, TDE's were determined for each atom type as shown graphically in Fig. 2. The rightmost data point for each species (shown in black) is a weighted average reflecting the multiplicity of the three directions studied. These average TDE values (70 eV for Sr, 140 eV for Ti, and 50 eV for O) are much greater than the recoil energy for ^{90}Sr computed above, where the average value is just 2.3 eV. Accordingly, the daughter species, ^{90}Y will be created *in situ* within the perovskite host, adopting the same position in the lattice as the parent. In the subsequent decay of ^{90}Y into stable ^{90}Zr, the recoil is considerably more energetic, reflecting the shorter half-life and higher Q-value for ^{90}Y. Even so, the average energy of the recoil from ^{90}Y decay, 25 eV, is still significantly less than the Sr TDE, which presumably is similar to that for Y, given that both occupy the A-site in

the perovskite crystal structure. Accordingly, the beta-decay of ^{90}Sr into ^{90}Zr is unable to generate defects via decay-induced recoil, and hence unusual chemistry is generated due to the presence of the notionally 4+ cation on the A-site of the perovskite (where Sr^{2+} typically resides). The chemical consequences of this substitution are explored in Section IV using density functional theory.

The abrupt chemical change leads to an additional effect known as "shake-off" in which the instantaneous change in the Coulomb potential perturns the electronic shells. [25, 26]. After transmutation the electrons are no longer in the ground state since the nuclear charge has changed by one. The average energy release associated with de-excitation processes can be estimated [25] and amounts to nearly 100 eV for both ^{90}Sr and ^{90}Y decay. While the fate of the daughter ion is strongly dependent on the local environment which can facilitate electronic rearrangement, such a large energy release can in principle lead to additional ionization (beyond that of the formally charge ion) and in turn the breaking of bonds. However, the quantification of such processes is exceedingly complex, and hence in our calculations we only consider the system in its ground state. Additionally, we also consider systems which are charge neutral, since the long half-life of the parent provides ample time for electronic recombination.

Another process which is difficult to quantify is the effect of the emitted beta particles on the host matrix. Two classes of interaction can occur: (i) electronic excitations induced by the passage of the high energy beta particle, and (ii) direct electron-ion collisions in which the kinematics are elastic. The latter effect has previously been examined in the context of ^{137}Cs decay in pollucite [27] and beam-damage [28] in apatite [29] using an electron microscope. Indeed, the energy of the electrons from an electron beam is not dissimilar to that of particles produced in beta-decay. One critical difference between beam damage and beta-decay is that the flux of beta particles is many orders of magnitude smaller than in a microscope, and hence radiation-induced Frenkel pairs in a beta-decay context are
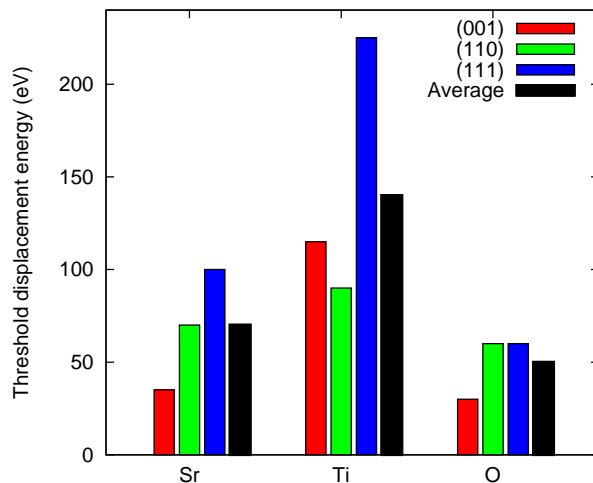

Figure 2. Threshold displacement energies (TDE's) from Thomas *et al.* [22] for SrTiO$_3$ as determined by molecular dynamics simulations along principle lattice directions.

in a much lower concentration and have the possibility of thermally activated recombination. Prediction of these recombination processes is extremely challenging, requiring methods such as Kinetic Monte Carlo [30], adaptive Kinetic Monte Carlo [31] and Temperature Accelerated Dynamics [32] which are not yet routinely applied to radiation damage problems; for an example of the latter see Ref. [33]. The only quantity which can be readily accessed is the maximum energy transfer for a beta particle with maximum energy colliding with an atom with an impact parameter of zero. In this limiting case scenario [27] (which is not representative of a typical electron-atom interaction within the solid), the maximum energy transferred to an atom in the host lattice is given by

$$E = \frac{2Q(Q + 2mc^2)}{Mc^2} \tag{8}$$

where M is the mass of the atom in the host. For Q=0.546 MeV as for ^{90}Sr decay, the maximum energy transfer is 21, 38 and 115 eV for Sr, Ti and O atoms, respectively. For Q=2.280 MeV as corresponding to ^{90}Y decay, the maximum energy transfer is rather higher, being 185, 338 and 1011 eV for Sr, Ti and O atoms, respectively. However, these quantities are absolute upper limits, and in a typical interaction the initial energy of the beta particle will be lower [according to the beta-decay spectrum, Fig. 1(a)], the collision will likely occur at a glancing angle (i.e. with a non-zero impact parameter), and the energy of the beta particle will reduce (as a function of time) due to successive interactions with the lattice. All of these effects combine to provide an average energy transfer much smaller than the upper theoretical limit.

In the case of inelastic processes, electronic excitation generates excited electrons in the conduction band and holes in the valence band. This initiates a complex series of process in which the energy which has been added to the electronic sub-system can either return to the lattice locally or be transported elsewhere via the migration of the holes and excited electrons. [34] Eventually the excited electrons and holes recombine, returning to the ground state by either radiative or non-radiative means. For metals the de-excitation time is extremely rapid (around 1 fs [13]), but in materials with a large band gap the recombination lifetime can be substantially longer. In radiative recombination the excited electrons and holes annihilate by emission of a photon, while in non-radiative recombination the energy is converted into phonons. In some materials the energy of these phonons is sufficiently large to create a defect, with the prototypical example being a Frenkel pair created by the decay of an exciton (i.e. a bound electron-hole pair) in an alkali halide. [13] Electronic excitation can also lead to damage other than point defects, such as phase transformations can be induced by collective local excitation of electrons which changes the potential energy surface of the atoms. [34] Yet another possibility for structural change is radiolysis, in which nuclei are ionized by the high-energy beta particle. In this process, new chemical environments are generated in which bonds are broken, potentially even leading to the release of gaseous products. Radiolytic effects in nuclear waste forms have concentrated mainly on effects in the aqueous state [35] or in alkali-halides [13]. Oxides such as $SrTiO_3$ are generally considered less susceptible to radiolysis than alkali-halides as the conditions required for bond-breaking are generally not met by oxides (see Ref. [13] for a discussion): all the same, relatively few studies have been performed. A comprehensive summary of modelling techniques to describe these electronic excitations is provided by Duffy *et al.* [34]. They note that, despite progress, understanding of the mechanisms and effects in many materials is far from complete.

As discussed earlier, these electronic effects typically take place far away from the transmuted atom, and accordingly we focus on chemical effects in the remainder of this study.

4. Chemical Evolution and Daughter Phases

We now turn to density functional theory (DFT) to quantify chemical evolution within two prototypical solids containing ^{90}Sr. We consider two notionally extreme parent phases, $SrTiO_3$ [Fig. 3(a)] for which the daughter Zr cation prefers the B-site occupied by Ti, rather than the A-site occupied by its parent, and SrH_2, for which the daughter phase ZrH_2 is very stable and well characterized. The choice of $SrTiO_3$ is motivated by the availability of TDE data and the use of perovskite phases in Synroc technology [36, 3] (although typically $CaTiO_3$ is used), while the choice of SrH_2 is purely conceptual, since a hydride-based wasteform would be unsuitable due to vulnerability to radiolysis.

4.1. Methodology

The majority of the DFT calculations were performed using the $DMol^3$ code [37] within the Materials Studio package available from Accelrys Software Inc. Exchange and correlation were treated using the PBE functional [38] and hydrogen and oxygen atoms were described within an all-electron framework. Valence and semicore electrons in Ti, Sr and Zr were described with DSPP pseudopotentials [39]. Double numerical basis sets with polarization functions are used for all atoms with a real-space cutoff of 5.8 Å. A `medium` quality integration grid (as defined within $DMol^3$) was used for all calculations of solids, while isolated atoms were evaluated using a `fine` integration grid. Reciprocal cell sampling of the Brillouin zone for the cubic $SrTiO_3$ and ZrH_2 structures used $12{\times}12{\times}12$ and $8{\times}8{\times}8$ k-point grids, respectively, with appropriate grids chosen for the other crystal structures and supercells by scaling these values as required. In all calculations we fully relax both the unit cell and atomic coordinates. Bader charge analysis was carried out using the `bader` program [40, 41] developed by the Henkelman group at the University of Texas, Austin. The `bader` program requires the full electron density since the presence of the cusp at the nucleus is an important component of the gradient-based algorithm used to construct the Bader volumes. This requirement poses a problem for pseudopotential calculations for which the core density is absent. Our solution to this problem is to augment the valence density with an Slater-type spherical charge density which reestablishes the cusp. We tested this approach using both $DMol^3$ and SIESTA [42] and obtained consistent results which were insensitive to the precise value of the Slater decay exponent.

A small number of DFT calculations were performed using the VASP program [43, 44] to study the dynamical stability of the $ZrTiO_3$ system. Imaginary phonon modes were computed using the `phonopy` program [45] using the same methodology as a related study of the $SrF_2 \rightarrow ZrF_2$ transformation [46]. All structures obtained by VASP were subsequently reoptimized within $DMol^3$. Structural trends were equivalent between the two packages; for clarity only the $DMol^3$ results are reported here.

4.2. Transmutation of $SrTiO_3 \rightarrow$ Perovskite $ZrTiO_3$

We have previously reported [47] preliminary results on the $Sr_{1-x}Zr_xTiO_3$ system, finding that the perovskite structure $ZrTiO_3$ is highly disfavored (≈ 0.45 eV/atom) relative to a phase-decomposed mixture of ZrO_2, TiO_2 and excess metal. Here we present a complete analysis of chemical evolution and structural quantities as a function of Zr concentration (x).

The starting point for assessing the phase stability of $Sr_{1-x}Zr_xTiO_3$ is the calculation of the perovskite end-member structures ($x=0$ and $x=1$) and the determination of the energetics of the phase-decomposed constituents. The two perovskite structures are shown in Fig. 3 and their computed properties are given in Table 1. When Sr (green spheres) are replaced with Zr (orange spheres) the lattice contracts slightly when the symmetry is constrained to be cubic. In a later section we will discuss the impact of breaking symmetry by following imaginary phonon modes. For the time being however, we will consider chemical evolution within a cubic perovskite lattice.

To assess the phase stability as a function of Zr concentration, we conceptually separate the $Sr_{1-x}Zr_xTiO_3$ phase into $SrTiO_3$ and $ZrTiO_3$ components, the latter of which is unstable with respect to some combination of ZrO_2, TiO_2, Zr metal and Ti metal. Lattice parameters and cohesive energies of these systems are provided in Table 1, and comparisons with other calculations and experiments are given. While the lattice parameters are generally in close agreement, cohesive energies can be non-trivial to calculate, particularly within DFT and especially so for metals. We have been very careful to ensure our calculations are converged and that the appropriate atomic reference has been used. To check our results we performed the same set of calculations using VASP (which uses a plane-wave basis set, rather than local orbitals as in DMol^3) and consistent results were obtained.

Using our cohesive energies for the phase decomposition products of $ZrTiO_3$, we can assess the relative stabilities of the reactions
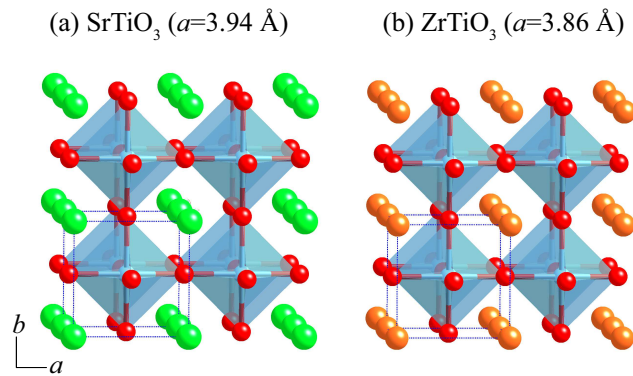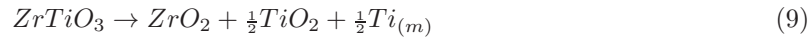
$$ZrTiO_3 \rightarrow ZrO_2 + \tfrac{1}{2}TiO_2 + \tfrac{1}{2}Ti_{(m)} \tag{9}$$

(a) SrTiO$_3$ (a=3.94 Å)   (b) ZrTiO$_3$ (a=3.86 Å)

Figure 3. Cubic perovskite crystal structures of (a) SrTiO$_3$, and (b) ZrTiO$_3$. Strontium, zirconium, titanium and oxygen atoms are shown as green, orange, blue and red-colored spheres, respectively. Calculations of the end-members used the 5-atom primitive shown by the box, while calculations of intermediate chemical compositions used the 40-atom cell as shown.

Table 1. Calculated and experimental structural properties of $SrTiO_3$, $ZrTiO_3$, TiO_2, ZrO_2, Ti metal and Zr metal. The cohesive energies (E_{coh}) for the metals have units of eV/atom.

System	E_{coh} (eV/f.u.)	a (Å)	b (Å)	c (Å)	β (°)
$SrTiO_3$ (cubic perovskite)					
- This Work	-33.166	3.938			
- HF [48]		3.940			
- GGA [49]		3.927			
- GGA [50]		3.946			
- Expt. [51, 52]		3.901			
$ZrTiO_3$ (cubic perovskite)					
- This Work	-34.430	3.862			
TiO_2 (rutile)					
- This Work	-21.379	4.646		2.982	
- HF [53]		4.575		2.929	
- GGA [53]		4.653		2.975	
- GGA [54]	-21.440	4.634		2.963	
- GGA [54]	-20.270	4.679		2.985	
- GGA [55]	-21.030	4.632		2.969	
- Expt. [56, 57]	-19.799	4.593		2.958	
ZrO_2 (monoclinic)					
- This Work	-23.182	5.202	5.289	5.361	99.44
- HF [58]		5.234	5.272	5.398	99.25
- GGA [59]		5.219	5.271	5.411	99.40
- GGA [55]	-21.610	5.200	5.262	5.331	99.46
- Expt. [60]	-22.822	5.150	5.212	5.317	99.23
Ti (hcp)					
- This Work	-5.771	2.934		4.675	
- GGA [61]	-5.870	2.940		4.642	
- GGA [62]		2.923		4.627	
- GGA [55]	-5.280	2.913		4.713	
- Expt. [63]	-4.850	2.950		4.680	
Zr (hcp)					
- This Work	-6.527	3.240		5.198	
- GGA [64]		3.250		5.207	
- GGA [55]	-6.430	3.228		5.132	
- Expt. [63]	-6.250	3.230		5.150	

$$ZrTiO_3 \rightarrow TiO_2 + \tfrac{1}{2}ZrO_2 + \tfrac{1}{2}Zr_{(m)} \tag{10}$$
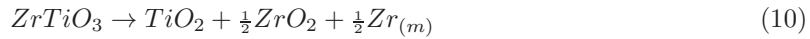
from which we find that Eq. 9 is exothermic by 2.33 eV per formula unit, while Eq. 10 is exothermic by 1.80 eV per formula unit. Accordingly, the phase decomposition of $ZrTiO_3$ favors the former reaction involving excess Ti metal.

A total of five intermediate structures were considered between the two end-members, using values of x=0.125, 0.25, 0.5, 0.75 and 0.875. Within the 40-atom supercell this corresponds to 1, 2, 4, 6, and 7 Zr atoms, respectively. For the structures with more than one symmetry-unique configuration, the minority cation was placed as far away as possible from atoms of the same type. Figure 4 shows the volume and cohesive energy as a function of the Zr concentration, with the latter expressed in eV/atom due to the conceptual complexity of defining a formula unit in dissimilar systems. As might be expected, the volume exhibits a simple linear trend which
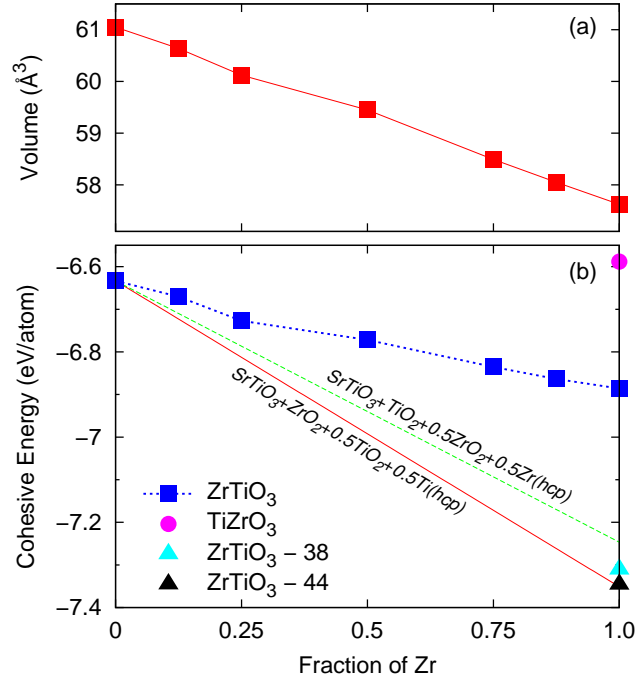
Figure 4. (a) Cell volume and (b) cohesive energy of the $Sr_{1-x}Zr_xTiO_3$ structures as a function of Zr concentration. Square data points denote Zr substitution on the A-site of the cubic perovskite. Circles denote a cubic perovskite structure with Zr on the B-site and Ti on the A-site, while triangles refer to orthorhombic $ZrTiO_3$ structures belonging to either spacegroup 38 or 44. Red and green lines denote two possible phase decomposition reactions involving excess Ti metal and Zr metal, respectively (Eqs. 9 and 10).

effectively interpolates between the two end-members. Although the Zr ionic radius for a formal charge of 4+ is around 30% smaller than that of Sr, the volume change is only 5%. This reflects both the role of the TiO_6 octahedra (which significantly contribute to the overall volume) and the unusual environment of the Zr cation (which results in a lower oxidation state as discussed below using Bader charges).

Figure 4(b) presents the cohesive energy for a variety of structures (solid points) as well as the two phase decomposition scenarios according to Eqs. 9 & 10 (straight lines). The squares denote Zr substitutions on the A-site and show that with Zr substitution the perovskite structure is increasingly unstable with respect to phase decomposition. The circle and triangles indicate three further Zr–Ti–O structures in which no Sr is present. The least stable structure is $TiZrO_3$ in which Ti occupies the A-site and Zr occupies the B-site. This anti-site configuration (shown as a circle) is significantly less stable than the structure shown in Fig. 3(b) in which Zr is on the A-site following transmutation of the ^{90}Sr.

Our calculations are supported by related work by Jaffe *et al.* [8] who used two DFT packages (VASP and SeqQUEST [65]) to study various Zr defects in $SrTiO_3$. In particular, they calculated defect formation energies for Zr substitution on the A-site for concentrations x of 0.125, 0.0625, 0.03704 and 0.03125. The first of these
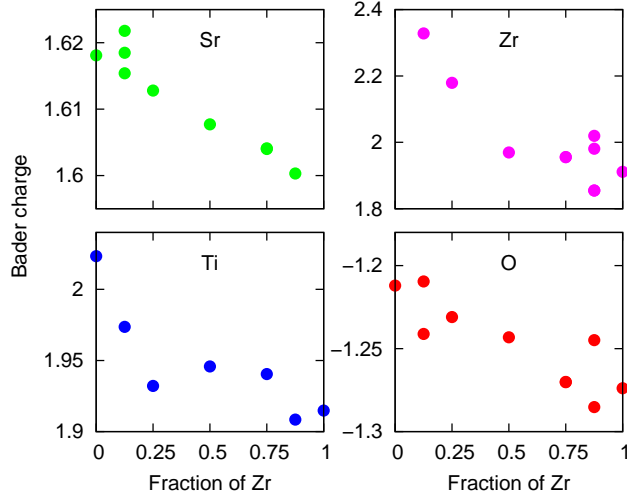
Figure 5. Bader charges for Sr, Zr, Ti and O atoms as a function of Zr concentration for $Sr_{1-x}Zr_xTiO_3$ cubic perovskite structures. Multiple values for a particular atom at a certain concentration indicate the presence of more than one symmetry-unique atom of this type in the structure.

concentrations directly overlaps with our work, where the equivalent quantities are 3.38 eV in this work, as compared to 3.39 eV using SeqQUEST and 3.50 eV using VASP. The work of Jaffe *et al.* thus complements our study, providing a detailed analysis of the low concentration regime while our study characterizes the pathway to full substitution.

To quantify the electronic changes associated with transmutation we computed Bader charges for all of the perovskite structures. Figure 5 shows the effect of Zr concentration on the constituent species of the perovskite phase. For the $SrTiO_3$ end-member the Bader charges are $+1.62$ for Sr, $+2.02$ for Ti and -1.21 for O. These values are consistent with partial charge pair potential models [23] for $SrTiO_3$ in which Sr is mostly ionic and Ti is less so. With increasing Zr concentration the Bader charges vary in a manner which are slightly counter-intuitive. Given the well-known ability of Ti to adopt both 3+ and 4+ oxidation states, one might have expected that the Bader charge of the Ti atom would significantly decrease to accommodate the increasing amounts of Zr. Instead, we observe the largest changes for the Zr itself, with the Bader charge reducing by around 20% over the entire range; in contrast, the Bader charge of the Ti cation reduces by only 5%. The Sr cation is largely unaffected by the presence of Zr species on the shared A-site (the Bader charge varies by less than 0.02 e^-), while the O anions gain a small additional electron density, consistent with the higher oxidation state of Zr^{4+} relative to Sr^{2+}. In a variety of other systems (e.g. TiO_2, ZrO_2, Ti_2O_3) we have observed Bader charges of around -1.2 for oxygen, suggesting a general insensitivity of the oxygen Bader charge in titanate-based materials. We note that this value is very similar to the empirically-determined partial charge of -1.096 employed in the widely-used Matsui and Akaogi potential [66] for TiO_2; this suggests that Bader charges might provide a useful starting point for the parametrization of partial charge models.

4.3. Relaxation of Perovskite ZrTiO₃→ Orthorhombic ZrTiO₃

Having shown that the perovskite $ZrTiO_3$ structure is significantly unstable with respect to phase decomposition, we investigated dynamical stability by computing the phonon dispersion relation along high symmetry directions. By following these modes we identified a series of connected structures with greatly increased stability; the cohesive energy of two of these structures are denoted by triangles in Fig. 4. Both structures (labelled $ZrTiO_3$–38 and $ZrTiO_3$–44 in the figure) have orthorhombic symmetry and are not perovskites; quite unexpectedly, the more stable of the two is only very slightly disfavored relative to the preferred phase decomposition. Although all geometry optimization and mode-following was performed in VASP, the coordinates and lattice parameters were again optimized in DMol^3 to generate the energies shown in Fig. 4(b). Results from both of the electronic structure packages were in very close agreement.

The starting point for the identification of the orthorhombic phases is cubic perovskite $ZrTiO_3$ which has a significant number of imaginary modes [Fig. 6(a)], the largest being $9.256i$ THz at the M-point. Following this mode by displacing the atoms according to the eigenvector yielded an orthorhombic structure with symmetry $Amm2$ (space group 38). Further mode-following at the Γ-point yielded a second orthorhombic structure belonging to the same space group; the triangular data point labelled as space group 38 in Fig. 4(b) corresponds to this second structure. The final mode-following procedure employed the phonon mode at the R-point, yielding a dynamically stable orthorhombic structure with $Imm2$ symmetry (space group 44). This final structure is only 0.005 eV/atom less stable than the phase-decomposed combination of ZrO_2, TiO_2 and metallic Ti. This result (which falls within the limits of accuracy in DFT) was completely unanticipated and highlights the unconventional nature of radioparagenesis. While conventional synthesis does not produce $ZrTiO_3$ compounds, it would be extremely instructive to seek alternative techniques to experimentally verify this theoretically-predicted compound. We predict that such a material would be a conducting oxide due to the finite density of states at the Fermi level observed in the DFT calculations (Fig. 7). As can be seen from the Figure, the Ti atoms provide the dominant contribution to the finite density of states at the Fermi level.

A polyhedral representation of the stable $ZrTiO_3$ compound is shown in Fig. 8; the corresponding lattice parameters are $a = 4.115$ Å, $b = 9.844$ Å and $c = 6.706$ Å. The Ti atoms are located in a triangular bipyramid formed by O atoms, and hence each Ti atom is coordinated to five O atoms. Such a five-fold environment is atypical for Ti but not unknown [67, 68]. The Zr atoms are also coordinated within an unusual polyhedral environment, possessing six O neighbours in two different octahedral arrangements. The base of the Zr1-centered octahedron, formed by the Zr1-O4 and Zr1-O5 bonds, is almost a square since the Zr1-O4 bond is shorter than Zr1-O5 by only 0.01 Å. In addition, the angle between O4, Zr1 and O1 atoms is about 88.5°. In the case of the Zr2-centered octahedron, the angle between O6, Zr2 and O7 atoms is 76.0° and the octahedron base, defined by the Zr2-O6 and Zr2-O2 bonds, is far from square in shape since the Zr2-O6 bond is larger than the Zr2-O2 bond by 0.18 Å. Bond lengths between the atoms involved in the triangular bipyramid and octahedrons are presented in Table 2. The Zr1-O1 bond with a length of 2.060 Å is the shortest bond in the two different Zr octahedrons and as shown in Fig. 8, it links the Zr1-centered octahedrons in a row along the a-direction. The distance between Ti and O2 atoms, 1.862 Å is
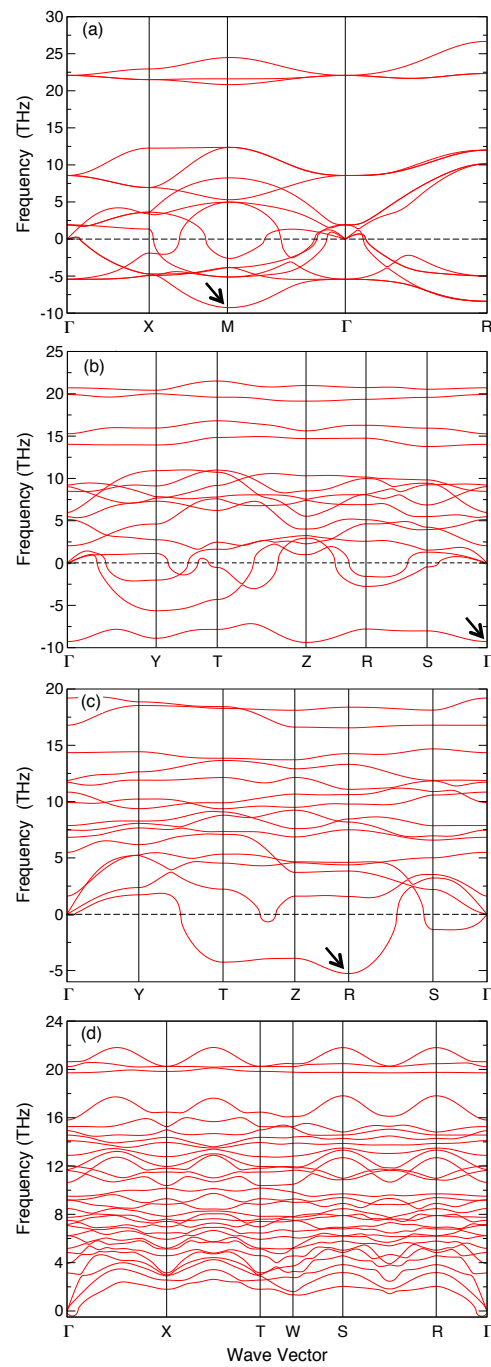
Figure 6. Phonon spectra for the ZrTiO$_3$ series of structures beginning with the unstable perovskite [panel (a)], the two orthorhombic structures in space group 38 [panels (b) and (c)], and the final stable orthorhombic structure in space group 44 [panel (d)]. The mode followed to access each subsequent structure is indicated by the arrow.
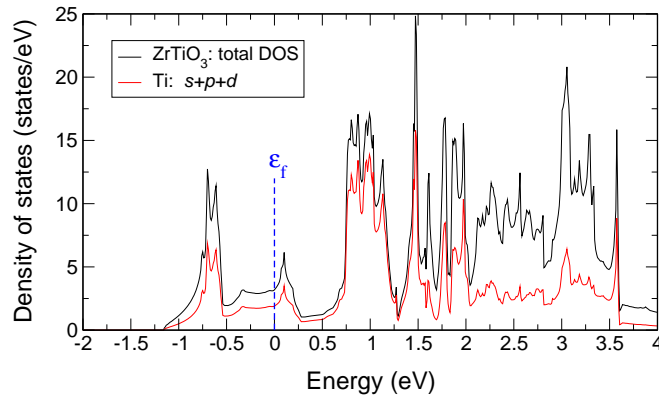
Figure 7. (color online) Density of states (DOS) near the Fermi energy for the orthorhombic $ZrTiO_3$ structure with the *Imm*2 (space group 44) symmetry. The total DOS is shown by the black line (upper of the two curves), while the red line (lower curve) shows the total Ti contribution.
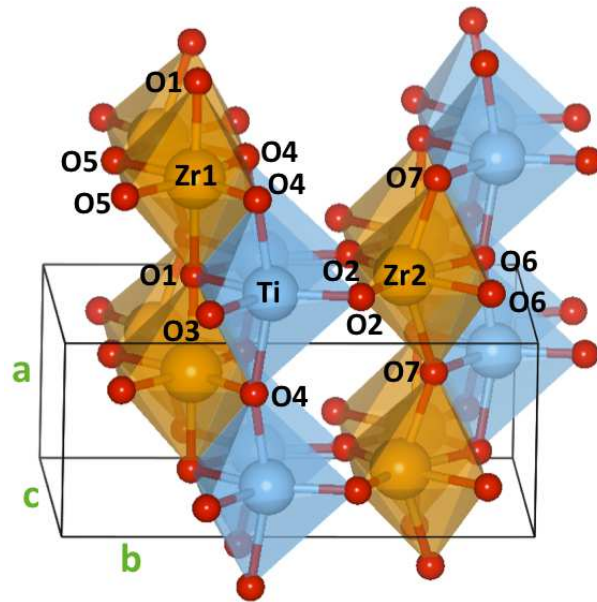

Figure 8. Crystal structure of the orthorhombic $ZrTiO_3$ structure with the *Imm*2 (space group 44) symmetry. Zirconium, titanium and oxygen atoms are shown as orange, blue and red-colored spheres, respectively, with symmetry-unique atoms also labelled.

the shortest amongst the whole crystal structure and it is the only contact that links Zr–Ti–O planes along the *b*-direction.

The Bader charges of the orthorhombic $ZrTiO_3$ structures were computed and are compared to the perovskite $ZrTiO_3$ and anti-site perovskite $ZrTiO_3$ structures in Fig. 9. Comparing the perovskite data with the ortho-44 data reveals a significant rearrangement of electronic charge due to relaxation; the Zr charge becomes significantly higher and the Ti charge is correspondingly reduced. The oxygen charge

Table 2. Structural parameters of orthorhombic $ZrTiO_3$ possessing $Imm2$ symmetry (space group 44).

Polyhedron	Quantity	Bond length (Å)
Triangular bipyramid	Ti - O1	2.116
	Ti - O2	1.862
	Ti - O3	2.264
	Ti - O4	2.110
Octahedron Zr1	Zr1 - O1	2.060
	Zr1 - O4	2.152
	Zr1 - O5	2.160
Octahedron Zr2	Zr2 - O2	2.102
	Zr2 - O6	2.286
	Zr2 - O7	2.176

remains largely unaltered (on average), continuing the trend noted earlier that the oxygen charge is relatively insensitive to structure. In the perovskite $ZrTiO_3$ structure the Zr and Ti atoms have almost identical Bader charges (about +1.9), consistent with notional oxidation states of +3 for both cations. However, in the relaxed (ortho-44) structure the Ti cation has a much smaller Bader charge than Zr, suggestive of Ti^{2+} and Zr^{4+} oxidation states. The anti-site perovskite structure exhibits much the same behavior, consistent with a +4 oxidation state for the Zr cation on the B-site, with a +2 state for the Ti cation in the A-site occupied by Sr^{2+} in the parent $SrTiO_3$ phase.

4.4. Transmutation of $SrH_2 \rightarrow ZrH_2$

As a second example of solid-state transmutation involving ^{90}Sr we now consider a hydride system in which both the parent and daughter phases are known structures. Such pairings are relatively uncommon due to the contrasting ionic size and radius of formally-charged Sr and Zr. For such a system it is not essential to consider phase decomposition since the transmuted daughter structure is chemically reasonable.

The parent SrH_2 phase adopts the cotunnite ($PbCl_2$-type) structure [Fig. 10(a)] in which the cation is nine-fold coordinated within an orthorhombic unit cell [69, 70]. An alternative anion-centred view [71] identifies two polyhedral environments; a tetrahedron (with four cations at the vertices and the anion at the centre), and a square pyramid (with five cations at the vertices surrounding the anion). Cotunnite is structurally related to fluorite; with common fluorite phases such as CaF_2, SrF_2 and BaF_2 (in each of which the cation is eight-fold coordinated) adopting the cotunnite phase at high pressure. In the fluorite structure, each anion sits in an ideal tetrahedron comprising four cations.

The daughter ZrH_2 phase adopts a face-centred-tetragonal phase [Fig. 10(b)] which can be considered as a uniaxially stretched fluorite lattice. In DFT studies of hydrogen embrittlement in zirconium, Ackland [72] predicted a stable tetragonal phase with $c/a > 1$, but the consensus view from experiments [73, 74] and other computational studies [75, 76, 77] is that the stable phase in fact has $c/a < 1$. Our own calculations are in agreement with the latter view.

In assessing the $SrH_2 \rightarrow ZrH_2$ transmutation, we explored four structures for each stoichiometry; cotunnite, fluorite, and the two tetragonal phases ($c/a < 1$ and $c/a > 1$). The fluorite structure provides a natural link between cotunnite-structured SrH_2
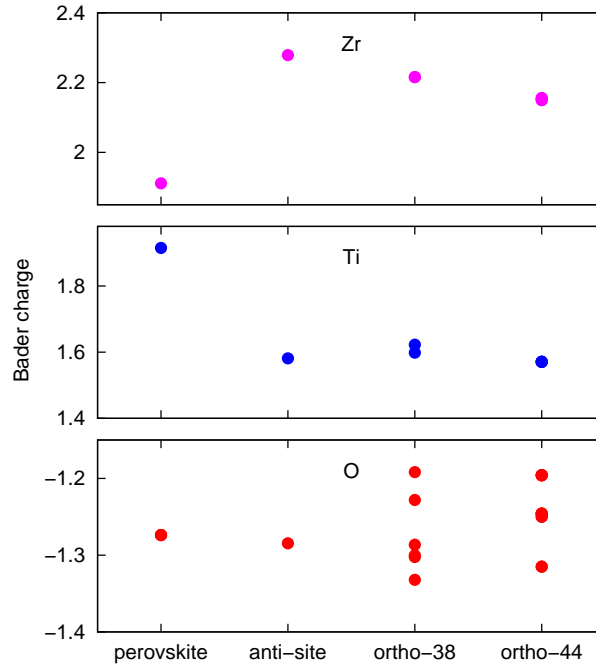
Figure 9. Bader charges for Zr, Ti and O atoms in Zr–Ti–O structures including the $ZrTiO_3$ cubic perovskite, $TiZrO_3$ anti-site and the orthorhombic $ZrTiO_3$ structures with *Amm*2 and *Imm*2 symmetry (spacegroups 38 and 44, respectively). Multiple values for a particular atom indicates there is more than one symmetry-unique atom of this type in the structure.
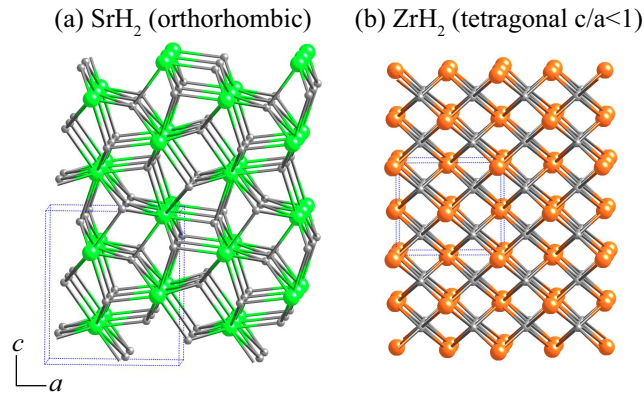
(a) SrH_2 (orthorhombic)   (b) ZrH_2 (tetragonal c/a<1)

Figure 10. Crystal structures of (a) orthorhombic SrH_2 and (b) tetragonal (c/a <1) ZrH_2, with strontium, zirconium and hydrogen atoms shown as green, orange and grey-colored spheres, respectively.

and the tetragonal-structured ZrH_2, and suggests an intuitive pathway along which the transformation would occur during chemical evolution. Accordingly, we do not consider mode-following of phonons for this system. In Table 3 we report the energetic

Table 3. Calculated structural properties and cohesive energies of SrH$_2$ and ZrH$_2$.

System	E$_{coh}$ (eV/f.u.)	a (Å)	b (Å)	c (Å)	c/a
SrH$_2$ (cotunnite/orthorhombic)					
- This Work	-7.765	6.414	3.868	7.356	
- GGA [70]	-7.610	6.350	3.850	7.290	
- HF [78]		6.364	3.875	7.343	
- Expt. [79]		6.371	3.862	7.319	
SrH$_2$ (fluorite)					
- This Work	-7.687	5.900			
ZrH$_2$ (cotunnite/orthorhombic)					
- This Work	-12.308	5.654	3.109	6.142	
ZrH$_2$ (tetragonal c/a <1)					
- This Work	-12.736	5.000		4.410	0.882
- LDA [76]		5.008		4.419	0.883
- Expt. [74]		4.975		4.447	0.894
ZrH$_2$ (tetragonal c/a >1)					
- This Work	-12.729	4.645		5.139	1.106
- LDA [76]		4.635		5.157	1.113
ZrH$_2$ (fluorite)					
- This Work	-12.711	4.809			
- LDA [76]		4.804			
- Expt. [74] (ZrH$_{1.62}$)		4.780			

stability and structural parameters for the parent and daughter phases. For SrH$_2$ we found that the tetragonal phases were indistinguishable from the fluorite and hence only the latter is reported. For ZrH$_2$ all four structure types are distinct, with all but the fluorite structure being local minima.

As shown in Table 3, we find that the stable phase of SrH$_2$ is the cotunnite structure, and our structural parameters are very similar to experimental and other computational values. Fluorite-structured SrH$_2$ is less stable than cotunnite by only 0.08 eV/f.u., a result that is not unreasonable given that SrF$_2$ adopts the fluorite phase and that SrH$_2$ and SrF$_2$ are both examples of formal ionic solids. The discriminating factor for SrH$_2$ is the smaller size of the H$^-$ anion relative to F$^-$ which favors a higher packing density (9-fold coordinate cations in cotunnite vs 8-fold coordination in fluorite). We note also that the computed fluorite phase is less dense than cotunnite by around 12%; this behavior is intuitive given that cotunnite is the higher pressure phase of several of the fluorites.

The lower half of Table 3 reports properties of four forms of ZrH$_2$. The cotunnite structure is by far the least stable, being more than 0.4 eV/f.u. higher in energy. Within an ionic framework this behavior is explained by the much smaller radius of Zr relative to Sr, thereby favoring a lower cation coordination. The other three phases have very similar cohesive energies, with the tetragonal phase with c/a <1 the most stable. This result is in good agreement with previous results. While the fluorite structure is not a local minima (being unstable with respect to tetragonal distortion), the computed lattice parameter compares well with sub-stoichiometric ZrH$_x$ for which the fluorite form (also known as the δ phase) is stable for x in the range 1.55–1.65. Experimental measurements [74] yield values of 4.776 and 4.780 Å for x=1.55 and 1.62, respectively. Our slightly higher value of 4.809 Å for ZrH$_2$ is entirely consistent with the presence of additional hydrogen which would lead to a small expansion of
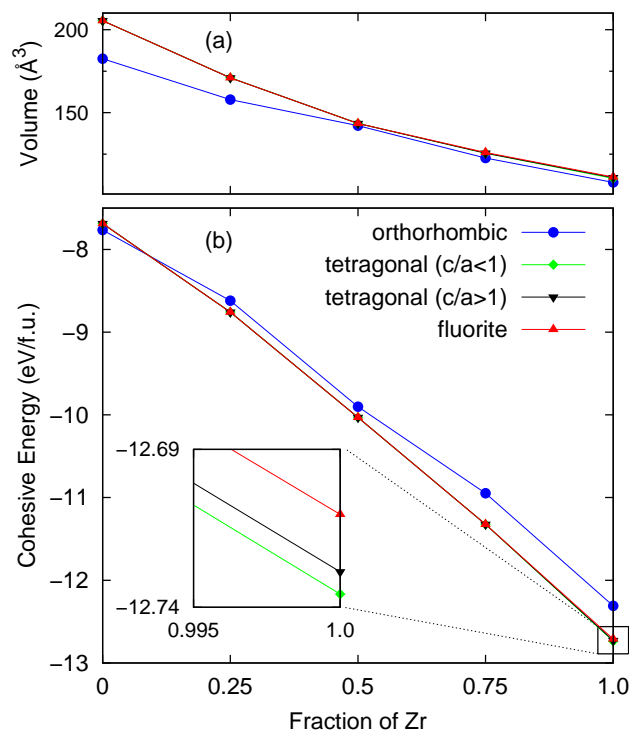
Figure 11. (a) Cell volume and (b) cohesive energy of the $Sr_{1-x}Zr_xH_2$ structures as a function of Zr concentration for the orthorhombic, tetragonal and fluorite structures. An inset is shown within panel (b) to highlight the most stable (lowest energy) structure.

the lattice.

Having established that we can satisfactorily describe the parent and daughter phases, we now consider mixed structures containing both Sr and Zr. All of the calculations (for the end-members as well as the mixed structures) employed 12-atom supercells, containing four cations and eight hydrogens. Accordingly, substitution of Sr with Zr yielded mixed structures with $x=0.25$, 0.5 and 0.75, where x is the fraction of Zr. In all of the structures, including cotunnite, there is only one cation environment and hence only one unique structure exists for $x=0.25$ and 0.75. For $x=0.5$ the substituted cations were maximally separated subject to the constraints of the supercell.

Chemical evolution in the $Sr_{1-x}Zr_xH_2$ system is summarized in Fig. 11. Both the volume and the cohesive energy vary approximately linearly between the two end-members. The dominant trend is competition between the cotunnite and fluorite structures, reflected in the large volume changes and the relative energetics. The tetragonal phases play a second-order role, emerging only in significance for the pure ZrH_2 system. For all other concentrations (i.e. $x\leq0.75$) the total energy of the fluorite and tetragonal phases were degenerate, indicating that only the fluorite structure was stable. The inset in Fig. 11(b) highlights just how small the energy differences are between the fluorite-related structures.

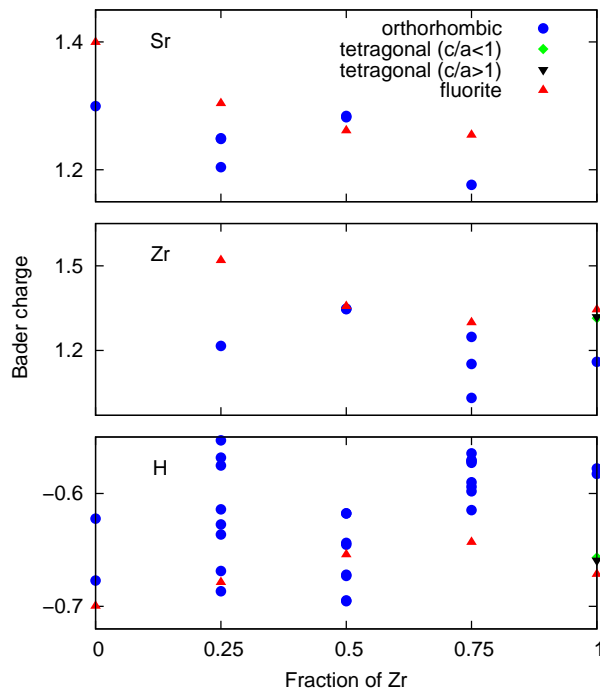The competition between cotunnite and fluorite is influenced by small amounts

Figure 12. Bader charges for Sr, Zr and H atoms as a function of Zr concentration for $Sr_{1-x}Zr_xH_2$ in the orthorhombic, tetragonal and fluorite structures. Multiple values for a particular atom at a given concentration indicates there is more than one symmetry-unique atom of that type in the structure.

of Zr, with fluorite already the favored phase at $x=0.25$ as seen in Fig. 11(b). This behavior can again be rationalised by the volume of the respective phase as shown in Fig. 11(a). At $x=0.25$ the fluorite phase is 8.3% larger in volume than cotunnite, whereas in the parent SrH_2 phase the same difference is 12.5%. As seen earlier in Table 3, fluorite SrH_2 is only slightly less stable than cotunnite. In the case of $Sr_{0.75}Zr_{0.25}H_2$ the smaller average cation size is sufficient to favor the 8-fold cation coordination present in fluorite.

An important observation from Fig. 11 is the very large increase in cohesive energy upon transmutation. The final ZrH_2 structure is 4.97 eV/f.u. (1.66 eV/atom) more stable than the parent SrH_2 structure. In contrast, the change in the cohesive energy upon transmutation of $SrTiO_3$ into $ZrTiO_3$ is just 0.25 eV/atom for the perovskite daughter phase and 0.71 eV/atom for the ortho-44 phase. The large energy gain seen for $SrH_2 \rightarrow ZrH_2$ transmutation is not particularly intuitive, especially given the large change in chemistry between Sr^{2+} and Zr^{4+}. This highlights the importance of employing DFT to explore chemical evolution involving disparate parent/daughter phases.

Figure 12 shows that the Bader charges for cations in the $Sr_{1-x}Zr_xH_2$ system differ significantly to those for chemical evolution in perovskite-structured $SrTiO_3$. Whereas Sr was predominantly ionic in $Sr_{1-x}Zr_xTiO_3$, with a Bader charge of around 1.6, the cotunnite SrH_2 ground-state has an Sr Bader charge of 1.3. With increasing chemical evolution, the Bader charge of Sr in the cubic phase remains around the

same value. Large differences between the oxide and hydride systems are also seen for Zr, with Bader charges of 1.9–2.3 in $Sr_{1-x}Zr_xTiO_3$, as compared to 1.3–1.5 in fluorite and tetragonal $Sr_{1-x}Zr_xH_2$. With the Bader charge of the hydrogen anion being very close to half that of oxygen, this difference can be attributed to the Ti cation whose Bader charge in the $SrTiO_3$ series is only 50% of the nominal formal charge value.

Although the Bader charges of the stable end-point structures (i.e. SrH_2 and ZrH_2) are reasonably similar, the electronic structure is quite different. Cotunnite-structured SrH_2 is a wide-gap insulator, with a DFT band-gap of around 3 eV (our HOMO-LUMO gap was 3.57 eV, while Hector *et al.* [70] report 2.812 and 3.211 eV for LDA and GGA calculations, respectively). In contrast, ZrH_2 is metallic with a finite density of states at the Fermi level [75]. As a result, chemical evolution from SrH_2 to ZrH_2 generates an insulator-metal transition between two stable structures. We are not aware of a link of this kind being previously noted.

5. Conclusion

In this work we have assessed the effect of beta-decay in three stages, considering first the energetics of the recoil process, secondly the creation of defects within the solid state, and thirdly the implications of chemical evolution on structural stability. The exposition of recoil energetics in Section II provides a relatively simple procedure for calculating the recoil of the daughter nucleus. While the precise values depend on the mass of the daughter and the shape and end-point of the beta spectrum, we see a general trend in which recoil energies vary from several eV up to, perhaps, several hundred eV. In the case of ^{137}Cs and ^{90}Sr as relevant to nuclear wasteforms, the average recoil energies are less than 10 eV, except for ^{90}Y which imparts several tens of eV to the nearby atoms. These values provide a guide to the extent of local damage beta-decay is likely to impart on a wasteform, and with the exception of a small number of studies [80, 81, 27, 82], this point has received little attention.

Section III outlined the companion concept to Section II, considering the creation of defects via energetic collisions. By considering the threshold displacement energy (TDE) in $SrTiO_3$, we showed that Sr→Y transmutation is unlikely to create a defect such as a Frenkel pair. Similarly, for the Y→Zr transmutation we infer that again a defect is not created due to the high TDE on the A-site. The absence of specific data for Y recoil in $SrTiO_3$ is symptomatic of a more general problem in that TDE data for most solids is often scant and difficult to calculate and/or measure. Robinson *et al.* [83] recently proposed a generalized methodology which provides a robust and reliable procedure for calculating TDE's in any kind of solid. This is a promising area of future work, with applications in a variety of related fields, most notably in ion-implantation where TDE values are an essential component of SRIM calculations used to interpret and model experimental studies. The effect of the beta particle on the surrounding material (which will typically be far away from the daughter) is another area where information on defect creation is lacking. Full treatment of this process requires a model to predict electronic excitation and recombination, as well as a probabilistic transport model using a package such as PENELOPE [84]. However, as noted by Duffy *et al.* [34], a full description of electronic excitations has yet to be achieved.

Chemical evolution induced by transmutation was quantified in Section IV, where for simplicity only bulk systems were considered. We focussed on daughter phases which were directly linked to the parent by either (i) direct substitution into known structures, or (ii) via phonon mode-following. Specifically, we did not consider random

structure searches to locate alternative phases with a given stoichiometry, nor did we consider processes such as defect migration, transient yttrium, or the role of surfaces and interfaces. Using two prototype parent phases, perovskite $SrTiO_3$ and cottunite SrH_2, we showed that chemical evolution can generate daughter phases which defy intuition. In the $SrTiO_3$ system we advanced our previous understanding [47], finding that phase decomposition can be avoided if the structure relaxes into an orthorhombic phase. This result was completely unexpected and could not have been anticipated. It continues the theme of interesting solid-state possibilities from radioparagenesis as first seen in the CsCl→BaCl system where an unusual rocksalt BaCl phase was identified via DFT [4]. The SrH_2 system evolves very differently to $SrTiO_3$ since the daughter phase is a known compound which is structurally related via an intermediate fluorite phase. In this case chemical evolution does not destabilize the solid phase, a result which is again somewhat counter-intuitive given the great difference between Sr^{2+} and Zr^{4+} cations. By employing Bader calculations we see in both systems local chemical environments which differ from traditional views of formal oxidation states.

Although the specific results in this paper relate to the particular case of ^{90}Sr decay in $SrTiO_3$ and SrH_2, the principles and concepts are applicable to a broad range of materials systems. Our analysis of recoil energetics, defect creation and chemical evolution is appropriate for any situation in which there is beta-decay of a major lattice constituent. Taken together, these three topics provide a framework for understanding radioparagenesis and identifying future directions such as synthesis of novel materials and accelerated chemical ageing in nuclear wasteforms.

Acknowledgments

References

[1] Ewing R C, Weber W J, and Clinard Jr. F W 1995 *Prog. Nucl. Energy* **29** 63
[2] Weber W J, Ewing R C, Catlow C R A, Diaz de la Rubia T, Hobbs L W, Kinoshita C, Matzke H, Motta A T, Nastasi M, Salje E K H, Vance E R, and Zinkle S J 1988 *J. Mater. Res.* **13** 1434
[3] Lumpkin G 2006 *Elements* **2** 365
[4] Jiang C, Stanek C R, Marks N A, Sickafus K E, and Uberuaga B P 2009 *Phys. Rev.* B **79** 132110
[5] Jiang C, Uberuaga B P, Sickafus K E, Nortier F M, Kitten J J, Marks N A, and Stanek C R 2010 *Energy Environ. Sci.* **3** 130
[6] Jiang C, Stanek C R, Marks N A, Sickafus K E, and Uberuaga B P 2010 *Phil. Mag. Lett.* **90** 435
[7] Jiang W, Bowden M E, Zhu Z, Jozwik P, Jagielski J, and Stonert A 2012 *Ind. Eng. Chem. Res.* **51** 621
[8] Jaffe J E, Van Ginhoven R M, and Jiang W 2012 *Comput. Mater. Sci.* **53** 153
[9] Jiang W, Van Ginhoven R M, Kovarik L, Jaffe J E, and Arey B W 2012 *J. Phys. Chem. C* **116** 16709
[10] Wigeland R A, Bauer T H, Fanning T H and Morris E E 2006 *Nucl. Technol.* **154** 95
[11] Robinson M T 1994 *J. Nucl. Mater.* **216** 1
[12] Krane K S 1988 *Introductory Nuclear Physics* (New York: John Wiley & Sons)
[13] Hobbs L J, Clinard Jr. F W, Zinkle S J, and Ewing R C 1994 *J. Nucl. Mater.* **216** 291
[14] Berger M J, Coursey J S, Zucker M A, and Chang J 2005 *ESTAR, PSTAR and ASTAR:*

Computer Programs for Calculating Stopping-Power and Range Tables for Electrons, Protons and Helium Ions (Version 1.2.3); available online at [http://physics.nist.gov/Star]

[15] Allen J S, Burman R L, Herrmannsfeldt W B, and Stähelin P 1959 *Phys. Rev.* **116** 134
[16] Johnson C H, Pleasonton F, and Carlson T A 1963 *Phys. Rev.* **132** 1149
[17] Beck M *et al* 2003 *Nucl. Instrum. Meth. Phys. Res.* A **503** 567
[18] Kozlov V Y *et al* 2006 *Int. J. Mass. Spectrom.* **251** 159
[19] Kozlov V Y *et al* 2008 *Nucl. Instrum. Meth. Phys. Res.* B **266** 4515
[20] Libby W F 1947 *J. Am. Chem. Soc.* **69** 2523
[21] Ziegler J F, Ziegler M D, and Biersack J P 2010 *Nucl. Instrum. Meth. Phys. Res.* B **268** 1818
[22] Thomas B S, Marks N A, and Begg B D 2007 *Nucl. Instrum. Meth. Phys. Res.* B **254** 211
[23] Thomas B S, Marks N A, and Begg B D 2005 *Nucl. Instrum. Meth. Phys. Res.* B **228** 288
[24] Benedek N A, Chua A L S, Elsässer C, Sutton A P, and Finnis M W 2008 *Phys. Rev. B* **78** 064110
[25] Serber R and Snyder H S 1952 *Phys. Rev.* **87** 152
[26] Levinger J S 1953 *Phys. Rev.* **90** 11
[27] Hess N J, Espinosa F J, Conradson S D, and Weber W J 2000 *J. Nucl. Mater.* **281** 22
[28] Egerton R F, Li P, Malac M 2004 *Micron* **35** 399
[29] Dong Z L, White T J, Wang L M, and Ewing R C 2005 *Microsc. Microanal.* **11** 2056
[30] Bortz A B, Kalos M H, and Lebowitz J L 1975 *J. Comput. Phys.* **17** 10
[31] Xu L and Henkelman G 2008 *J. Chem. Phys.* **129** 114104
[32] Sørensen M R and Voter A F 2000 *J. Chem. Phys.* **112** 9599
[33] Li Y H *et al.* 2012 *Phys. Rev. Lett.* **108** 195504
[34] Duffy D M, Daraszewicz S L, and Mulroue J 2012 *Nucl. Instrum. Meth. Phys. Res.* B **277** 21
[35] Weber W J, Pederson L R, Gray W J, and McVay G L 1984 *Nucl. Instrum. Meth. Phys. Res.* B **1** 527
[36] Ringwood A E, Kesson S E, Ware N G, Hibberson W, and Major A 1979 *Nature* **278** 219
[37] Delley B 2000 *J. Chem. Phys.* **113** 7756
[38] Perdew J P, Burke K, and Ernzerhof M 1996 *Phys. Rev. Lett.* **77** 3865
[39] Delley B 2002 *Phys. Rev. B* **66** 155125
[40] Bader W F W 1990 *Atoms in Molecules: A Quantum Theory* (New York: Oxford University Press)
[41] Tang W, Sanville E, and Henkelman G 2009 *J. Phys.: Condens. Matter* **21** 084204
[42] Soler J M, Artacho E, Gale J D, García A, Junquera J, Ordejón P, and Sánchez-Portal D 2002 *J. Phys.: Condens. Matter* **14** 2745
[43] Kresse G and Furthmüller J 1996 *Phys. Rev. B* **54** 11169
[44] Kresse G and Furthmüller J 1996 *Comput. Mater. Sci.* **6** 15
[45] Togo A, Oba F, and Tanaka I 2008 *Phys. Rev. B* **78** 134106
[46] Sassi M, Uberuaga B P, Stanek C R, and Marks N A 2012 *Phys. Rev. B* **85** 094104
[47] Uberuaga B P, Jiang C, Stanek C R, Sickafus K E, Marks N A, Carter D J and Rohl A L 2010 *Nucl. Instrum. Meth. Phys. Res.* B **268** 3261
[48] Piskunov S, Heifets E, Eglitis R and Borstel G 2004 *Comput. Mater. Sci.* **29** 165
[49] Ghebouli B, Ghebouli M A, Chihi T, Fatmi M, Boucetta S, and Reffas M 2009 *Solid State Commun.* **149** 2244
[50] Shein I R, Kozhevnikov V L, and Ivanovskii A L 2008 *Solid State Sci.* **10** 217
[51] Fischer G, Wang Z, and Karato S 1993 *Phys. Chem. Miner.* **20** 97
[52] Abramov Y A, Tsirelson V G, Zavodnik V E, and Ivanov S A 2008 *J. Chem. Theory Comput.* **4** 341
[53] Labat F, Baranek P, Adamo C, and Brown I D 1995 *Acta. Cryst.* B **51** 942
[54] Lazzeri M, Vittadini A, and Selloni A 2001 *Phys. ReV. B* **63** 155409
[55] Duan X M, Stampfl C, Bilek M M M, McKenzie D R and Wei S H 2011 *Phys. Rev. B* **83** 085202
[56] Lide D R 2003 *CRC Handbook of Chemistry and Physics* 81st Edition (London: CRC Press)
[57] Burdett J K, Hughbanks T, Miller G J, Richardson J W, and Smith J V J 1987 *J. Am. Chem. Soc.* **109** 3639
[58] Stefanovich E V, Shluger A L, and Catlow C R A 1994 *Phys. Rev. B* **49** 11560
[59] Zheng J Z, Ceder G, Maxisch T, Chim W K, and Choi W K 2007 *Phys. Rev. B* **75** 104112
[60] Howard C J, Hill R J, and Reichert B E 1988 *Acta. Cryst.* B **44** 116
[61] Da Silva J L F, Stampfl C, and Scheffler M 2006 *Surf. Sci.* **600** 703
[62] Pozzo M, Alfe D, Amieiro A, French S, and Pratt A 2008 *J. Chem. Phys.* **128** 094703
[63] Kittel C 1996 *Introduction to Solid State Physics* 7th Edition (New York: John Wiley & Sons)
[64] Pozzo M and Alfe D 2009 *Int. J. Hydrogen Energy* **34** 1922
[65] See http://dft.sandia.gov/Quest/

[66] Matsui M and Akaogi M 1991 *Mol. Sim.* **6** 239
[67] Whittle K R, Lumpkin G R, Blackford M, Aughterson R D, Smith K L, and Zaluzec N J 2010 *J. Solid State Chem.* **183** 2416
[68] Whittle K R, Blackford M G, Aughterson R D, Lumpkin G R, and Zaluzec N J 2011 *Acta Mater.* **59** 7530
[69] Smith J S, Desgreniers S, Klug D D, and Tse J S 2009 *Solid State Commun.* **149** 830
[70] Hector L G, Herbst J F, Wolf W, Saxe P, and Kresse G 2007 *Phys. Rev.* B **76** 014121
[71] Morris E, Groy T, and Leinenweber K 2001 *J. Phys. Chem. Solids* **62** 1117
[72] Ackland G J 1998 *Phys. Rev. Lett.* **80** 2233
[73] Ducastelle F, Caudron R, and Costa P 1970 *J. Phys. France* **31** 57
[74] Niedźwiedź K, Nowak B, and ŻogałO J 1993 *J. Alloys Compd.* **194** 47
[75] Gupta M 1998 *Phys. Rev. Lett.* **81** 3300
[76] Wolf W and Herzig P 2000 *J. Phys.: Condens. Matter* **12** 4535
[77] Domain C, Besson R, and Legris A 2002 *Acta Mater.* **50** 3513
[78] El Gridani A, Drissi El Bouzaidi R, and El Mouhtadi M 2000 *J. Mol. Struct. (Theochem)* **531** 193
[79] Ting V P, Henry P F, Kohlmann H, Wilson C C, and Weller M T 2010 *Phys. Chem. Chem. Phys.* **12** 2083
[80] Gray W J 1982 *Nature* **296** 547
[81] Vance E R, Roy R, Pepin J G, and Agrawal D K 1982 *J. Mater. Sci.* **17** 947
[82] Fortner J, Aase S, and Reed D, 2002 *Mat. Res. Soc. Symp. Proc.* **713** 527
[83] Robinson M, Marks N A, Whittle K R, and Lumpkin G R 2012 *Phys. Rev.* B **85** 104105
[84] Sempau J, Fernández-Varea J M, Acosta E, and Salvat F 2003 *Nucl. Instrum. Meth. Phys. Res.* B **207** 107